PAPER • OPEN ACCESS

Nonlinear optical signatures of ultraviolet light-induced ring opening in α-terpinene

New Journal of Physics
The open access journal for physics

Nonlinear optical signatures of ultraviolet light-induced ring opening in α-terpinene

Brantley A West[1], **Brian P Molesky**[2], **Nicholas P Montoni**[2] **and Andrew M Moran**[2,3]

[1] Department of Physics and Astronomy, The University of North Carolina at Chapel Hill, Chapel Hill, NC 27599, USA
[2] Department of Chemistry, The University of North Carolina at Chapel Hill, Chapel Hill, NC 27599, USA
E-mail: ammoran@email.unc.edu

New Journal of Physics **15** (2013) 025007 (21pp)
Received 2 August 2012
Published 5 February 2013
Online at http://www.njp.org/
doi:10.1088/1367-2630/15/2/025007

Abstract. Photoinduced electrocyclic ring opening reactions in conjugated cylcoalkenes are among the most elementary processes in organic chemistry. One prototypical ring opening reaction transforms cyclohexadiene into hexatriene. It is known that a sequence of sub-100 fs internal conversion transitions precedes bond breaking in cyclohexadiene and some of its derivatives. However, these excited state dynamics have never been directly monitored in solution because of insufficient time resolution. Here we aim to uncover the extraordinary photophysics behind related ultrafast internal conversion processes in a derivative of cyclohexadiene, α-terpinene (α-TP), solvated in cyclohexane. Transient absorption anisotropy experiments conducted with 20 fs laser pulses at 267 nm expose non-exponential depopulation kinetics for the $\pi\pi^*$ electronic state of α-TP. Our data show that population transfer rapidly accelerates within the first 100 fs after photoexcitation. In addition, recurrences in two-dimensional photon echo (2DPE) line shapes reveal strong vibronic coupling in a normal mode near 523 cm^{-1}, which involves torsions of the C=C bonds and hydrogen out-of-plane (HOOP) wagging on a vinyl group. With the support of several experiments, we hypothesize that the excited state wavepacket in α-TP undergoes several recurrences in the C=C stretching coordinate before

[3] Author to whom any correspondence should be addressed.

displacement along the C=C torsion/vinyl HOOP coordinate finally sets it free from the Franck–Condon region of the potential energy surface. The unconfined wavepacket departs the $\pi\pi^*$ electronic state by way of a conical intersection with a lower energy excited state. The present observations are made possible by recent improvements to both the time resolution and detection sensitivity of our experimental setup. This work demonstrates that it is now possible to acquire 2DPE signals in the deep ultraviolet, which are comparable with high-quality measurements in the visible spectral region. These technical developments open the door to studies of many beautiful models for elementary chemical dynamics.

Contents

1. Introduction

Among the most elementary processes in organic chemistry are electrocyclic ring opening reactions in which conjugated cycloalkenes are transformed into conjugated polyenes (e.g. cyclohexadiene (CHD) becomes hexatriene) [1, 2]. The stereospecificities of these reactions depend on whether they involve conrotatory or disrotatory twisting around the broken sigma bond. The Woodward–Hoffman rules leverage knowledge of nodes in the π molecular orbitals to predict the particular type of motion involved in the ring opening process [3, 4]. While very elegant and powerful, these rules conveniently hide many intricacies of the physics behind these reactions [5]. For example, research conducted on CHD shows that photoinduced ring opening is preceded by a sequence of sub-100 fs internal conversion transitions [5–16]. Details of these excited state dynamics have only recently come into focus in photo-ionization mass spectrometry experiments employing extraordinarily short ultraviolet (UV) laser pulses [8].

In this paper, we use femtosecond laser spectroscopies to investigate the excited state dynamics preceding ring opening in a derivative of CHD, α-terpinene (α-TP), whose structure is shown in figure 1. Similar relaxation processes are expected to follow photoexcitation in CHD and α-TP because the aliphatic substituents weakly perturb the conjugated π molecular orbitals in the ring [6, 8]. Given that similar behaviors are anticipated, it is useful to review

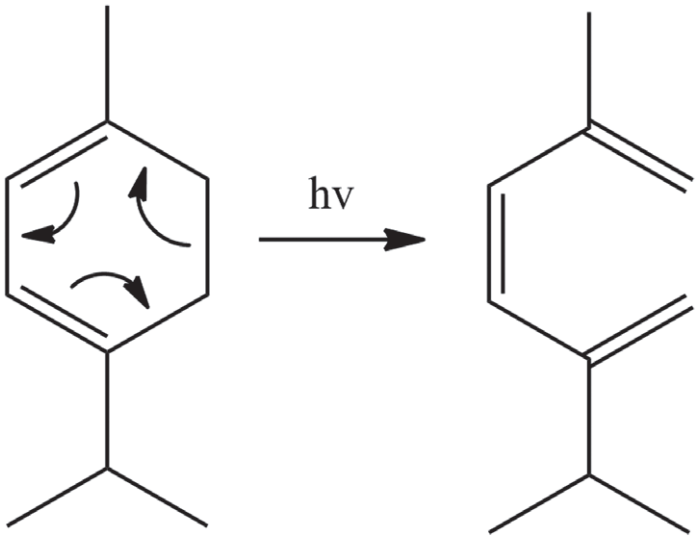

Figure 1. Photoinduced ring opening reaction of α-TP. This reaction scheme shows only one of the possible isomers generated through ring opening.

what is currently known about photoinduced relaxation in CHD [6–9]. Figure 2 presents a schematic representation of the relevant potential energy surfaces. Photoexcitation of the 1B state, which is a HOMO-to-LUMO transition, initiates (mostly) symmetric wavepacket motion toward a conical intersection with an optically forbidden 2A state characterized by a doubly occupied LUMO orbital. The internal conversion process between states 1B and 2A possesses a time constant of 55 fs. Subsequent electronic population transfer from state 2A to the ground state occurs in approximately 80 fs. Ring opening and out-of-plane symmetry-breaking motions are thought to occur near the conical intersection between the ground state and state 2A. Adiabatic relaxation in the ground electronic state then separates CHD from the hexatriene photoproduct, which forms with quantum efficiencies of 40% in solution [8, 17] and 100% in the gas phase [18]. The origin of the different reaction yields observed in the gas phase and solution is currently unknown [7].

The primary goal of this work is to uncover the physics behind analogous internal conversion transitions in α-TP. To facilitate comparisons with CHD, we will hereafter refer to the excited states of α-TP in the same notation shown in figure 2. Obviously, α-TP does not possess C_2 symmetry; however, its π molecular orbitals are similar to those in CHD. Notably, the ultrafast transition between the 1B and 2A states has never been directly monitored (in the time domain) for any member of the CHD family of molecules in solution because of insufficient time resolution. We see the direct attainment of time constants as a valuable contribution but also wish to address deeper physical questions. Sub-100 fs photoinduced electronic relaxation processes hold a special place in condensed phase dynamics because the environment that surrounds the system generally does not equilibrate on this time scale [19, 20]. Here we use the term *environment* to refer to all of the nuclear coordinates in the solute and the solvent which are relegated to a heat bath in a reduced quantum mechanical description. Traditional kinetic theories do not apply in the sub-100 fs regime because they generally assume that the bath maintains equilibrium throughout the process of interest. In essence, the key issue is that the correlation functions governing non-radiative transitions do not fully decay until a sufficient number of phase-randomizing collisions have occurred. Non-exponential population transfer is

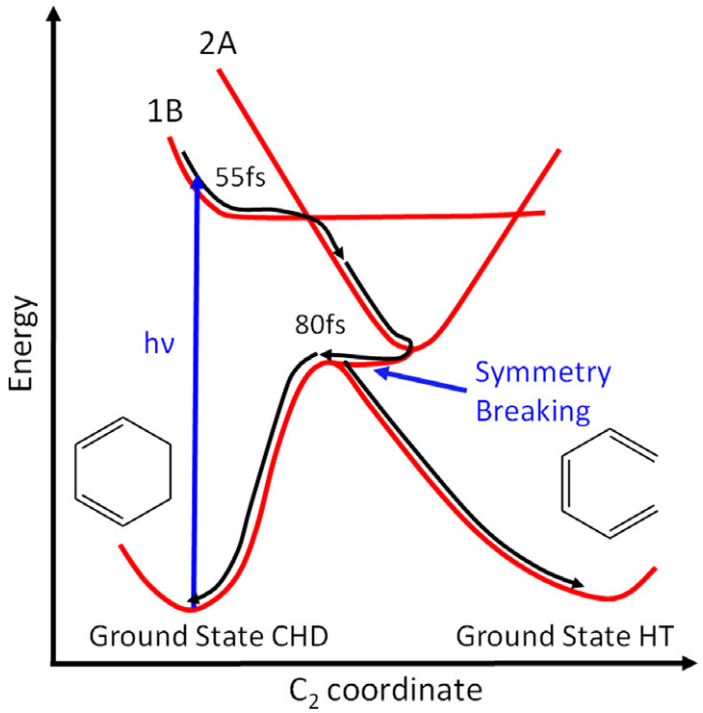

Figure 2. Relaxation scheme for CHD. Photoexcitation into the 1B state initiates (mostly) symmetric wavepacket motion toward a conical intersection with state 2A. State 2A transfers population to the ground state within 80 fs. Ground state recovery is accompanied by asymmetric nuclear motion. Roughly 40% of the photoexcitations produce hexatriene (HT) in solution (only one of the isomers is shown above). Similar dynamics are thought to mediate the ring opening process in α-TP. In this work, we refer to the electronic states of α-TP in the same notation in order to facilitate comparisons with CHD. This figure is adapted with the permission from [2]. Copyright 2010 American Chemical Society.

one consequence of this coincidence between the electronic and nuclear relaxation time scales. We examine the non-exponential internal conversion kinetics in α-TP with the goal of exposing the vibronic couplings from which such non-Markovian dynamics originate. The extraordinary physics associated with vibronic interactions at conical intersections make α-TP an excellent model for photophysical studies [21–23].

Compared to the gas phase, measurements in solution confront the additional problems of dispersion management and undesired nonlinearities in the sample medium. Propagation effects can be minimized by making the sample very thin (100 μm or less) [24]. However, it is generally not possible to probe dynamics during the region of laser pulse overlap, because the electronic polarizability of the solvent gives rise to a quasi-instantaneous 'coherence spike' [25–30]. Access to the sub-100 fs time scale is afforded only by minimizing the laser pulse durations and, in turn, the width of the coherence spike. Motivated by observations of extremely fast dynamics, the present study makes use of new improvements in the time resolution of our four-wave mixing apparatus. In earlier publications, we described the initial implementation of an argon-filled hollow-core waveguide capable of generating 25 fs laser pulses. The 800 cm^{-1} bandwidth

was sufficient to carry out two-dimensional photon echo (2DPE) spectroscopies on components of DNA [29–31]. However, this earlier setup required improvements in two areas. Firstly, the UV bandwidth was limited by the 180 fs duration of the 800 nm driving pulse derived from a titanium sapphire amplifier. Secondly, UV bandwidths much broader than 800 cm^{-1} could not be compressed because of residual third-order dispersion (TOD) accumulated in a prism compressor. In this work, we employ a laser system newly upgraded for 90 fs pulse durations at 800 nm and use mirrors that impart negative group delay dispersion for UV pulse compression. We are now able to observe dynamics at times as short as 40 fs following photoexcitation.

2. Experimental methods

2.1. Generation of 20 fs laser pulses with cross-modal phase matching in a hollow-core waveguide

It was shown more than a decade ago that broadband UV laser pulses are readily generated in argon-filled hollow-core fibers driven by sub-30 fs, 800 nm pulses [32–34]. These devices are typically configured to operate with each laser beam in the (lowest order) EH_{11} mode. EH_{11} modes couple well to laser beams with Gaussian spatial profiles at the entrance to the fiber and are subject to less attenuation than higher order modes [35, 36]. For these reasons, such auto-modal phase matching (AMP) is generally desirable because it yields (low-order) UV pulses with the greatest efficiency. Cross-modal phase matching (CMP) describes four-wave mixing processes wherein the three laser beams occupy different modes. CMP has been discussed but, to our knowledge, never systematically leveraged as a means of optimizing the UV bandwidth. Indeed, AMP should be preferred when extremely short near-infrared laser pulses are available for pumping an apparatus. Limitations to AMP were explored by Bradforth and co-workers who found that 25 fs pulse durations are still attainable with AMP (i.e. all beams in EH_{11}) and 100 fs, 800 nm driving pulses [37]. In this section, we show that CMP can be exploited to generate 20 fs pulse durations despite beginning with 180 fs pulses at 800 nm. The attainment of extraordinary bandwidths with modest resources suggests that short UV pulses will become readily available.

In our setup, 40 μJ pulses at 400 and 800 nm are focused into a hollow-core fiber with a diameter of 75 μm [29, 31]. The UV (267 nm) pulse energies range between 150 and 800 nJ depending on the alignment and pressure. Here we compare the UV bandwidths achieved before and after a recent upgrade to our laser system in which the pulse duration at 800 nm was reduced from 180 to 90 fs by switching from fiber oscillator seed pulses to Ti:sapphire seed pulses. In figure 3, the UV bandwidths are plotted versus pressure before and after the upgrade. The 800 nm beam propagates in the lowest order mode, whereas the 400 nm beam is forced to propagate in a higher order mode by slightly misaligning it from the fiber axis. Notably, four well-resolved peaks in the bandwidth are observed below 900 Torr. Corresponding peaks in the pulse energy are evident but are not as pronounced. In these measurements, we first optimized the bandwidth at 850 Torr and then scanned the pressure without modifying the alignment. Thus, measurements made before and after the upgrade can be directly compared. This procedure is probably why the pulse energy and bandwidth do not exhibit identical profiles (i.e. the pulse energy and stability are not re-optimized at each pressure). Nonetheless, the well-resolved peaks in the bandwidth signify the pressures at which phase matching occurs. For our purposes, it is most important that the EH_{11} UV mode generated at 850 Torr possesses a spectral width that

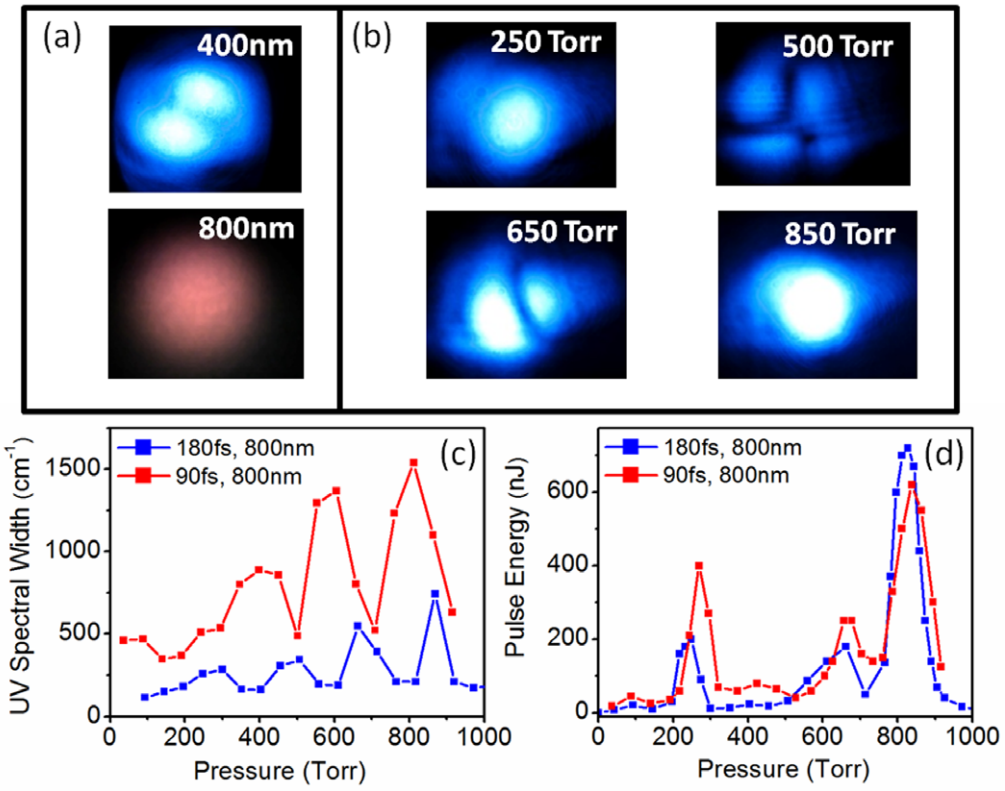

Figure 3. (a) Photographs of the 400 and 800 nm beams at the exit of the hollow core fiber at 850 Torr. (b) Photographs of the 267 nm laser beam at the fiber exit at four pressures where phase matching is observed. The full-width at half-maximum spectral widths (c) and pulse energies (d) at 267 nm are plotted with respect to the pressure in the fiber. The blue and red points, respectively, correspond to measurements carried out with 180 and 90 fs pulses at 800 nm.

is more than twice as large as that produced with AMP at 250 Torr. We attribute the broader bandwidth afforded by CMP to enhanced self-phase modulation at higher pressures.

The particular modes associated with the four nonlinearities observed in figure 3 can be assigned by examining the phase mismatch for the process. The wavevector for light propagation within the fiber is given by [33]

$$k(\lambda, P) = \frac{2\pi n(\lambda, P)}{\lambda}\left[1 - \frac{1}{2}\left(\frac{u_{nm}\lambda}{2\pi a}\right)^2\right], \tag{1}$$

where $n(\lambda, P)$ is the refractive index of argon (λ is the wavelength and P is the pressure), a is the fiber radius and u_{nm} is the modal constant. Phase matched UV generation is achieved under the condition $\Delta k = 2k_{400} - k_{800} - k_{267}$, where the laser wavelengths are written as subscripts. Table 1 summarizes the particular modes associated with each of the four peaks observed in the UV bandwidth. The CMP process employed in our experiments is calculated at 790 Torr and measured at 800–850 Torr. It is predicted that 800 and 400 nm input beams, respectively, propagate in EH_{12} and EH_{31} modes, whereas the 267 nm UV beam occupies the lowest order EH_{11} mode. The 800 nm beam generally appears Gaussian at the exit of the fiber due to the

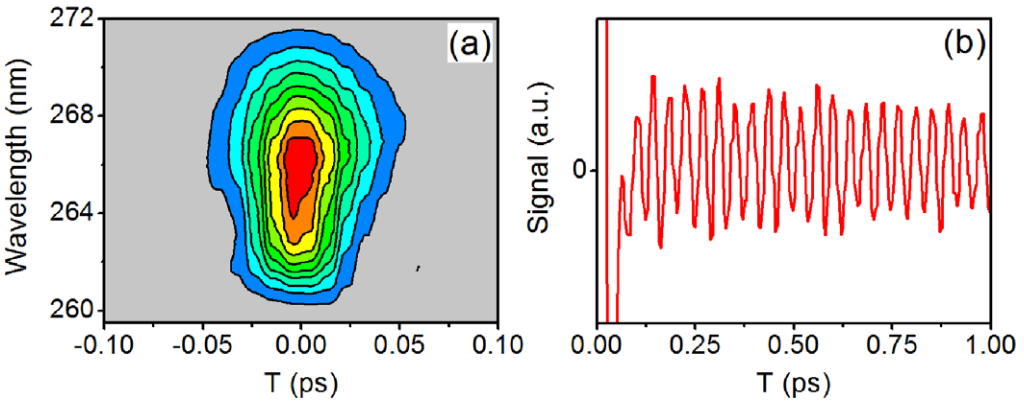

Figure 4. (a) TG signal amplitude measured in cyclohexane with 20 fs laser pulses at 267 nm. (b) The dispersive part of the transient grating signal field reveals oscillations with a 42 fs period, which correspond to a Raman active vibrational mode of cyclohexane [68].

Table 1. Summary of the phase matching conditions for argon-filled hollow-core fiber.

Pressure (Torr) measured	Pressure (Torr) calculated	EH mode at 800 nm	EH mode at 400 nm	EH mode at 267 nm
250	253	EH_{11}	EH_{11}	EH_{11}
500	390	EH_{23}	EH_{33}	EH_{23}
650	640	EH_{11}	EH_{11}	EH_{21}
850	790	EH_{31}	EH_{12}	EH_{11}

relative attenuation of higher order modes. However, higher order 400 nm modes are observable at the exit of the fiber under CMP conditions. We note that propagation of the 400 nm pulse in the EH_{31} mode is nominally forbidden for laser beams with (free-space) Gaussian profiles, but this restriction is relaxed when the laser beam is detuned from the fiber axis [35].

Of course, the broad UV bandwidth afforded by CMP is useful only if it can be compressed. In this work, we utilize a dual compressor composed of fused silica prisms (85 mm separation) and a pair of mirrors that impart negative group delay dispersion (Femtolasers). Prototypes for these mirrors were characterized in earlier work [38]. Our chirped mirror compressor is configured for 40 reflections with s-polarized laser beams. Figure 4 presents a transient grating spectrogram acquired with cyclohexane wherein a vibrational coherence with a 42 fs period is impulsively excited. The laser pulses have time–bandwidth products of approximately 0.45. Our analysis suggests that the positive TOD accumulated in the prism compressor is nearly fully compensated for by negative TOD imparted by dielectric mirrors (CVI, TLM1), waveplates and prism wedges. One drawback associated with CMP at 800–850 Torr is that multiple modes are more readily produced in the UV. Fortunately, the suppression of multi-mode operation is relatively straightforward because this condition usually gives rise to several distinct peaks in the UV laser spectrum.

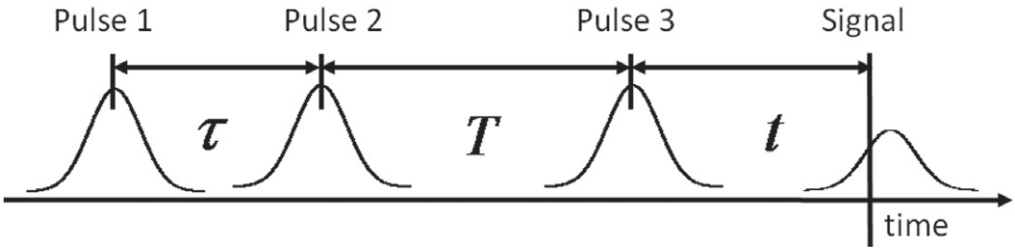

Figure 5. Pulse sequence used in TG and 2DPE spectroscopies. Photoexcitation of the system takes place during the experimentally controlled delay, τ; internal conversion and ring opening dynamics occur during the population time, T; the signal is radiated in the emission time, t. TG experiments scan T with $\tau = 0$, whereas 2DPE uncovers correlations in the excitation and emission frequencies, ω_τ and ω_t, at various T. All three pulses are centered at 37 500 cm^{-1} and have 20 fs durations. This figure is adapted with permission from [29]. Copyright 2011 American Chemical Society.

2.2. Transient grating and photon echo spectroscopies

Transient grating (TG) and 2DPE experiments involve a sequence of three laser pulses whose delay times are defined in figure 5. TG measurements use a motorized translation stage to scan T (with $\tau = 0$), the interval in which internal conversion and ring opening dynamics occur. 2DPE additionally scans τ from -100 to $+100$ fs (at various T) by moving fused silica prism wedges in the paths of pulses 1 and 2 [39]. Fourier transformation with respect to τ yields the excitation dimension of the 2DPE spectrum, ω_τ; the emission dimension, ω_t, is obtained by dispersing the signal pulse in the spectrometer. The 2DPE signals of α-TP fully decay by $|\tau| = 40$ fs because the $\pi\pi^*$ resonance possesses a broad line width. The amount of glass associated with a delay of 40 fs stretches a 20 fs laser pulse at 267 nm by less than 0.02 fs. Therefore, the dispersion associated with displacements of the wedges has a negligible effect on the two-dimensional (2D) line shape.

A diffractive optic-based interferometer described in an earlier publication is used to carry out TG and 2DPE experiments [29]. In this setup, the diffractive optic generates a boxcars laser beam geometry in which signals are collected under the phase matching condition $\mathbf{k}_S = -\mathbf{k}_1 + \mathbf{k}_2 + \mathbf{k}_3$. Three of the laser pulses induce nonlinear polarization, whereas the fourth (attenuated) pulse is used as a reference field for signal detection by spectral interferometry [40, 41]. In all experiments, signals are detected using a back-illuminated CCD array (Princeton Instruments PIXIS 100B) mounted on a 0.3 m spectrograph with a 3600 g mm^{-1} grating. Integration times range between 100 and 200 ms and are adjusted based on the signal intensity.

TG anisotropy measurements are carried out by interleaving sets of five scans with parallel and perpendicular pump and probe electric field polarizations. A total of 20 scans are collected for each tensor element. Signal amplitudes for the two tensor elements are also compared at various delay times to ensure that the value of the anisotropy is correct. We conservatively estimate that this procedure results in an uncertainty of 0.04 in the anisotropy. The polarization condition is varied by rotating a half-waveplate in the path of the 'pump' laser beam (i.e. pulses 1 and 2).

Solutions of α-TP are prepared in cylcohexane with optical densities of 0.8 in a 100 μm path length. We do not observe signal contributions from the solvent at $T > 40$ fs with this optical density. 2DPE spectra are corrected for propagation effects using established procedures [24]. The optical density of the solution has a minor effect on the 2DPE line shapes because the linear absorption coefficient changes slightly within the laser bandwidth [29]. The sample solution, which has a volume of 50 ml, is flowed through a gravity-fed jet with 100 μm path length [42]. The use of the jet minimizes dispersion and significantly suppresses scattered light (compared to a cuvette). Absorbance spectra are measured before and after the experiments to confirm the absence of sample degradation. Each of the three incoming laser pulses used in the TG and 2DPE experiments has a fluence of approximately 3.8×10^{13} photons cm^{-2} and a peak power of 1.4 GW cm^{-2}. We estimate that approximately 0.2% of the molecules are photoexcited using the sum of the fluences for pulses 1 and 2. Low pulse energies must be employed because high peak powers, which scale as the inverse of the pulse duration, can readily induce (undesired) ionization of the solute and the solvent [29].

3. Results and discussion

3.1. Analysis of linear absorption line shapes

In this section, line broadening mechanisms are delineated in α-TP by modeling the absorbance spectrum. The absorbance line shape encodes information on solute–solvent interactions, Franck–Condon progression in the intramolecular modes and excited state lifetimes. To extract this information, the spectrum is simulated using a framework for the optical response wherein vibronic coupling is incorporated with Brownian oscillator coordinates. Two such modes are sufficient to fit the absorbance spectrum of α-TP. Firstly, we consider the fluctuations in the $\pi\pi^*$ resonance frequency imposed by thermally driven motions of the solvent and low-frequency intramolecular vibrations. The spectral density associated with this overdamped motion is written as [20]

$$C_{\mathrm{OD}}(\omega) = 2\lambda \frac{\omega\Lambda}{\omega^2 + \Lambda^2}, \tag{2}$$

where λ is the reorganization energy and Λ^{-1} is the time scale of the bath. Secondly, it is known that the C=C stretching mode dominates the higher-frequency intramolecular part of the vibronic response in CHD and its derivatives [15, 43]. Contributions from other vibrations, whose couplings are much smaller, cannot be uniquely parameterized based on the absorbance spectrum alone (i.e. resonance Raman data would be needed). We therefore incorporate only the C=C stretching mode using the (underdamped) spectral density [20]

$$C_{\mathrm{UD}}(\omega) = \frac{1}{2} d^2 \omega_v^2 [\delta(\omega - \omega_v) - \delta(\omega + \omega_v)], \tag{3}$$

where d is the dimensionless displacement and ω_v is the mode frequency. The two components of the spectral density are added together, $\mathrm{C}(\omega) = C_{\mathrm{OD}}(\omega) + C_{\mathrm{UD}}(\omega)$, and the line broadening function is generated with

$$g(t) = \frac{1}{2\pi} \int_{-\infty}^{\infty} \mathrm{d}\omega \frac{1 - \cos(\omega t)}{\omega^2} \coth(\beta\hbar\omega/2) C(\omega) + \frac{\mathrm{i}}{2\pi} \int_{-\infty}^{\infty} \mathrm{d}\omega \frac{\sin(\omega t) - \omega t}{\omega^2} C(\omega). \tag{4}$$

Table 2. Fitting parameters for the linear absorbance line shape.

Parameter	Non-exponential lifetime broadening	Exponential lifetime broadening
$\omega_{\pi\pi^*}$	34130 cm^{-1}	34100 cm^{-1}
λ	1500 cm^{-1}	1150 cm^{-1}
Λ^{-1}	100 fs	100 fs
ω_v	1450 cm^{-1}	1450 cm^{-1}
d	1.98	1.98
[(a)] γ^{-1}	50 fs	33 fs
[(a)] b	4.47	1.00

[(a)] Lifetime broadening parameters, γ and b, are taken directly from the measured anisotropy decay.

With $g(t)$ in hand, the linear absorbance line shape is computed using

$$\sigma_A(\omega) = \int_0^\infty dt \exp\left[i(\omega - \omega_{\pi\pi^*})t - g(t) - (\gamma t)^b\right], \tag{5}$$

where $\omega_{\pi\pi^*}$ is the $\pi\pi^*$ electronic transition frequency (i.e. electronic origin), γ reflects depopulation of the $\pi\pi^*$ state and b governs the shape of the population decay. The transition dipole is not used as a fitting parameter because we are interested in the information encoded in the absorbance line shape (not the magnitude of the extinction coefficient).

The measured and calculated absorbance spectra are shown in figure 6, and the fitting parameters are given in table 2. The Franck–Condon progression associated with the C=C stretching mode is clearly evident despite the fairly broad line width of α-TP. This aspect of the spectrum differs from CHD where the vibronic structure is unresolved because of the extremely short $\pi\pi^*$ lifetime [6, 15, 44]. The absorbance spectrum is fit by constraining the reorganization energy, λ, to be consistent with the value obtained in an earlier resonance Raman intensity analysis for CHD [15]. The frequency and displacement of the C=C stretching mode are then determined based on the vibronic progression in the spectrum. In parameterizing the solvation rate, Λ, we take into account the 2DPE measurements presented below, which show that a component of the bath relaxes on the 100 fs time scale. The linear absorbance spectrum is weakly affected by the time scale of the bath, Λ^{-1}, when it is greater than 50 fs. The low-energy tail of the absorbance spectrum is quite sensitive to the population decay parameters, γ and b. We fit the spectrum under the assumptions of both non-exponential ($b \neq 1$) and exponential ($b = 1$) dynamics. The lifetime broadening parameters are taken directly from the analysis of transient absorption anisotropy data presented below in order to minimize the number of adjustable degrees of freedom. First, b is set equal to the value determined with a direct fit of the anisotropy ($b = 4.47$). The fit is quite reasonable and the lower-frequency side of the calculated spectrum agrees well with the measurement. The spectrum calculated with $b = 1.0$ is also in fair agreement, but overestimates the Lorentzian character in the 32 000–34 000 cm^{-1} range. Notably, these fits focus on the line shape below 38 000 cm^{-1} because of interference with a higher energy resonance. This portion of the spectrum provides adequate constraints for the parametrization of the model.

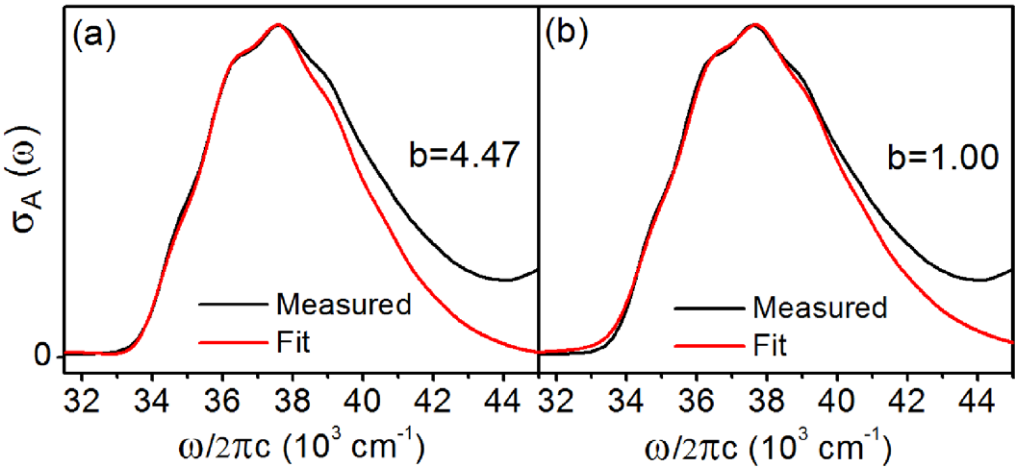

Figure 6. Measured (black) and calculated (red) absorbance spectra for α-TP. The data are fit under the assumption of both (a) non-exponential and (b) exponential population decay. Absorbance spectra are computed using equation (5) and the fitting parameters are given in table 2. These fits focus on the absorbance line shape below 38 000 cm^{-1} because of interference with a higher energy resonance.

Non-exponential population decay should come as no surprise for α-TP and other derivatives of CHD because their internal conversion rates are comparable with the fastest nuclear relaxation processes (e.g. solvation and intramolecular vibrational energy redistribution). In the reduced description of quantum mechanics often employed for condensed phases, rate constants are defined as the time integrals of correlation functions involving the operator that couples the initial and final states [19, 20, 23]. Processes that take place on time scales for which such integrals have not fully converged generally do not exhibit exponential kinetics. Nuclear motions in condensed phases span a broad range of frequencies and time scales, so predictions regarding exponential versus non-exponential kinetic behavior can be difficult to make in some cases. However, the internal conversion transition in α-TP is so fast that it competes even with the sub-100 fs dephasing processes that govern the absorbance line shape. It is certain in α-TP that internal conversion takes place on a time scale where the nuclei are still adjusting to the presence of the $\pi\pi^*$ excitation.

3.2. Probing internal conversion dynamics with transient absorption anisotropies

In this section, we probe internal conversion dynamics in α-TP using transient absorption signals obtained as the absorptive parts of TG signal fields. The measurements are carried out with both parallel and perpendicular pump and probe electric field polarizations in order to isolate the electronic relaxation process (i.e. suppress the contributions from nuclear relaxation). The anisotropy generated using these tensor elements is sensitive to electronic relaxation because the dipoles connecting different pairs of electronic states in a molecule generally have different orientations [45–47]. Sensitivity to the internal conversion process in α-TP derives from excited state absorption (ESA) nonlinearities because the laser spectrum is resonant with only state 1B (i.e. the $\pi\pi^*$ electronic state). The key point is that depopulation of the 1B state

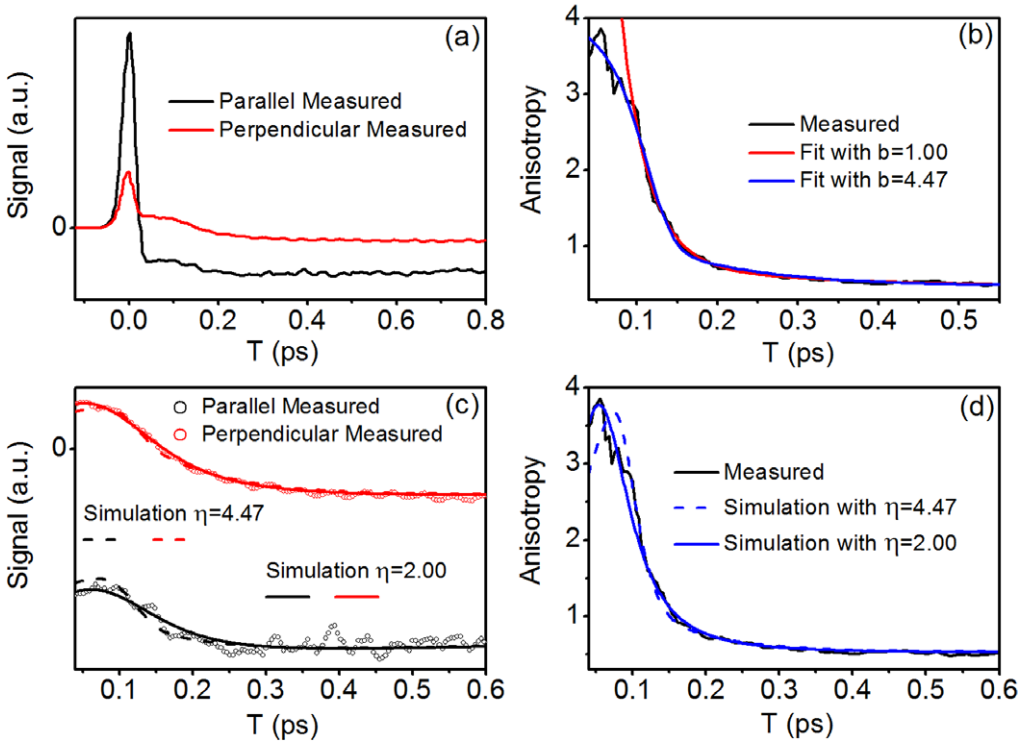

Figure 7. (a) Absorptive (real) parts of TG signal fields measured for α-TP with parallel (black) and perpendicular (red) pump and probe polarizations. In this representation, signals with positive and negative signs correspond to a photoinduced absorption and bleach, respectively. (b) The measured anisotropy is fit under the assumption of (red) exponential and (blue) non-exponential relaxation dynamics. Fitting parameters are given in table 3. (c) TG signals acquired with parallel and perpendicular pump and probe polarizations are simulated using equations (A.11) and (A.12) with the parameters given in table 4. (d) The measured and the calculated anisotropies are compared. The parameter, η, captures the non-exponential shape of the population decay, whereas b possesses small contributions from nuclear dynamics. These data suggest that the depopulation of state 1B follows a Gaussian-like temporal profile.

occurs concomitant with the decay of the component of the optical response associated with ESA. Internal conversion causes the signal field polarization to rotate because ESA possesses contributions from resonances with transition dipole orientations different from the transition dipole connecting the ground state to the 1B excited state.

Transient absorption signals acquired with both parallel, $S_{\parallel}(T)$, and perpendicular, $S_{\perp}(T)$, polarizations are presented in figure 7. $S_{\parallel}(T)$ bleaches instantly following the 'coherence spike' at $T = 0$, whereas $S_{\perp}(T)$ changes sign near $T = 200$ fs. This sign change is an indication that ESA nonlinearities contribute to the response at short delay times. The anisotropy is first generated with

$$r(T) = \frac{S_{\parallel}(T) - S_{\perp}(T)}{S_{\parallel}(T) + 2S_{\perp}(T)}, \tag{6}$$

Table 3. Fitting parameters for transient absorption anisotropies.

Parameter[(a)]	Non-exponential decay	Exponential decay
A_0	0.48 ± 0.02	0.47 ± 0.02
A_1	2.27 ± 0.28	36.6 ± 4.9
τ_1 (fs)	120 ± 3	33 ± 2
b	4.47 ± 0.58	1.00 ± 0.00
A_2	1.39 ± 0.46	0.54 ± 0.18
τ_2 (fs)	130 ± 20	189 ± 48

[(a)] Ranges in the fitting parameters correspond to twice the standard error.

and then fit using the following function:

$$F(T) = A_0 + A_1 \exp[-(T/\tau_1)^b] + A_2 \exp(-T/\tau_2). \tag{7}$$

$F(T)$ includes both an exponential term and a term in which the exponent, b, enables non-exponential behavior. This phenomenological function is motivated by its ability to distinguish exponential and non-exponential behaviors with a minimum number of parameters.

The anisotropy is fit both with b as a free parameter and with b set equal to 1.0 (see table 3). The full shape of the decay is captured with $b = 4.47$, whereas only the dynamics after $T = 0.15$ ps are well described using $b = 1.0$. For example, note that the fit of the anisotropy with $b = 1.0$ diverges at $T = 0.10$ ps. We assign the non-exponential term to population transfer from state 1B to state 2A. Assignment of the 130 fs time constant is not as straightforward. One interpretation is that it reflects the return of population from state 2A to the ground state. In this scenario, the anisotropy derives sensitivity to the depopulation of state 2A through a resonance between state 2A and a higher energy excited state. A second possibility, which we consider less likely, is that the anisotropy reflects only the depopulation of state 1B. In this interpretation, the two decay components would correspond to distinct sub-populations prepared by photoexcitation. Simulations of wavepacket dynamics in α-TP, similar to those carried out on CHD [48, 49], will be helpful in establishing a detailed microscopic interpretation of the measured dynamics.

The anisotropy is simulated using the model outlined in appendix A to further explore the origin of the dynamics in the signal polarization. Decomposing the nonlinear response function into individual terms more directly addresses the temporal profile associated with depopulation of state 1B because the parameter b in equation (7) may possess contributions from fast nuclear relaxation. Our model aims to capture the 'true' non-exponential character of the population dynamics with η. As in equation (7), it is assumed that the two decay components, τ_1 and τ_2, respectively, represent depopulation of the 1B and 2A electronic states. The model also introduces an inertial solvation time constant, τ_{solv}, and a vibrational cooling time, τ_{VC}, associated with the formation of an open-chain photoproduct. In figure 7, the signals are fit with η set equal to both 4.47 and 2.00 in order to evaluate the extent to which the population dynamics differ from the directly measured shape of the anisotropy decay (where $b = 4.47$). The fits are reasonable in both cases but are slightly better with $\eta = 2.00$ at $T < 0.15$ ps, which suggests that the internal conversion process is indeed non-exponential. The model calculations also make clear that the anisotropy decay convolves the depopulation of state 1B with the inertial

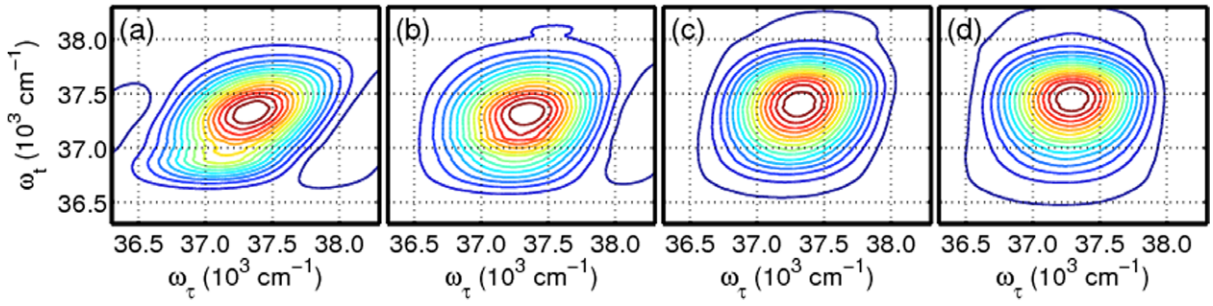

Figure 8. (a) Absorptive (real) parts of 2DPE spectra acquired for α-TP at (a) $T = 100$ fs, (b) $T = 125$ fs, (c) $T = 225$ fs and (d) $T = 500$ fs. The magic angle polarization condition is employed.

part of the solvation process. Based on the analysis of the data summarized in appendix B, we conservatively suggest that the true dynamics may range anywhere between $\eta = 1.7$ and 3.2. Most importantly, these simulations support the interpretation that state 1B is depopulated in a non-exponential fashion.

3.3. Signatures of solvation dynamics in photon echo line shapes

The anisotropy measurements presented above are primarily sensitive to electronic relaxation. In this section, we use 2DPE spectroscopy to investigate the nuclear dynamics initiated by photoexcitation. It was established in the first 2D electronic spectroscopy experiments that solvation induces a loss of correlation between the excitation, ω_τ, and detection, ω_t, frequencies [50]. In essence, the 2DPE line shape becomes more circular in appearance as the local solvent geometry loses memory of its initial structure. The present measurements examine similar signatures of solvent reorganization. In addition, the fast internal conversion transitions in α-TP give rise to vibrational cooling processes in the ground electronic state, which also influence the 2DPE line shapes.

2DPE spectra acquired at delay times ranging from $T = 100$ to 500 fs are presented in figure 8. The spectrum at $T = 100$ fs possesses an elongated shape signifying correlation between ω_τ and ω_t. Solvation gradually washes out these correlations until the spectrum acquires the fairly circular appearance found at $T = 500$ fs. To analyze the dynamics in the line shapes, we fit diagonal ($\omega_\tau = \omega_t$) and anti-diagonal ($-\omega_\tau = \omega_t$) slices of the 2D spectra and plot the ratio of Gaussian widths, Γ_{ad}/Γ_d, with respect to T in figure 9. A fit to a sum of two exponentials reveals processes with 19.8 and 36.8 ps time constants. The robust conclusion to be drawn is that distinct classes of dynamics take place on time scales near 100 fs and in the tens of picoseconds range. The shorter time constant is assigned to reorganization of the solvent and intramolecular vibrational energy redistribution. Because the overall time scales for these processes are generally greater than 20 fs, we suggest that the measurement is primarily sensitive to the departure of the wavepacket from the Franck–Condon geometry. The 36.8 ps time constant, which is not well determined because the range of the fit does not extend beyond $T = 500$ fs, most likely represents solute-to-solvent vibrational energy transfer in the ground electronic state. Evolution in the 2DPE line shapes at $T < 200$ fs confirms that internal conversion and nuclear relaxation processes occur simultaneously in α-TP. The non-exponential

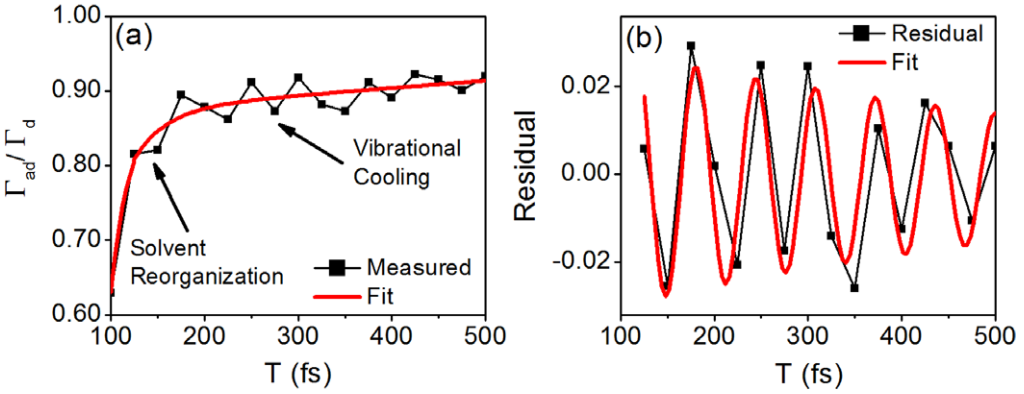

Figure 9. (a) The ratio in the anti-diagonal, Γ_{ad}, and diagonal, Γ_d, 2DPE line widths obtained for α-TP with magic angle polarizations. The ratio is fit using $F(T) = A_0 + \sum_{i=1}^{2} A_i \exp(-T/\tau_i)$, where $A_0 = 1.35$, $A_1 = -0.45$, $\tau_1 = 19.8$ fs, $A_2 = -0.48$ and $\tau_2 = 36.8$ ps. (b) The residual corresponding to panel (a) is fit using $F(T) = A_0 + A_1 \exp(-T/\tau_{\text{damp}}) \sin[2\pi(T - T_c)/w]$, where $A_0 = -0.010$, $A_1 = 0.026$, $T_C = 36.4$ fs, $\tau_{\text{damp}} = 590$ fs and $w = 63.7$ fs. The 523 cm^{-1} recurrence is assigned to a vibrational mode involving both C=C torsion and HOOP motion on the vinyl group. This suggests that the 523 cm^{-1} mode possesses a large excited state potential energy gradient (on the 1B surface) at the equilibrium geometry of the molecule.

internal conversion kinetics exhibited by α-TP are a natural consequence of this coincidence in time scales.

Figure 9 reveals a coherent quantum beat in the 2DPE line shape. The residual of the fit in panel (a) is fit with a damped sine function. The recurrence in Γ_{ad}/Γ_d corresponds to a vibrational mode with a wavenumber of 523 cm^{-1}. Strong vibronic coupling implies that the vibration probably involves motion of the ring (not the substituents) in the vicinity of the $\pi\pi^*$ excitation. Thus, the modes of CHD, which are well characterized, are a natural starting point for making an assignment in α-TP. The C=C torsion (507 cm^{-1} in CHD) and hydrogen out-of-plane (HOOP) wagging mode on the vinyl group (562 cm^{-1} in CHD) are the most likely candidates [15]. A computational normal mode analysis conducted on α-TP at the B3LYP/6311G(d) level yields a vibration at 528 cm^{-1} with both HOOP and C=C torsion character (the calculation is performed in a dielectric cyclohexane medium using the integral equation formalism version of the polarizable continuum model) [51]. Therefore, we assign the 523 cm^{-1} recurrence in α-TP to a normal mode composed of both vinyl HOOP and C=C torsion motions.

Detection of the 523 cm^{-1} mode indicates that it is associated with a steep potential energy gradient in the 1B state at the equilibrium geometry (i.e. the Franck–Condon activity). These recurrences must represent wavepacket motion in the ground electronic state because they persist at delay times, T, that are long compared to the lifetime of the 1B state [20]. Thus, the coherent dynamics displayed in figure 9 have a different origin than those detected in photo-ionization mass spectrometry experiments on CHD where excited state wavepacket motions are interrogated [8]. Finally, we note that this quantum beat is not detected in the TG or 2DPE amplitudes. 2DPE electronic spectroscopies applied to other systems have similarly exposed coherent beats in the 2D line shapes [52–54]. The present observation underscores the power

of 2DPE spectroscopy for uncovering relaxation processes that are hidden from conventional techniques [50, 55–64].

4. Concluding remarks

The present investigation of photoinduced relaxation processes in α-TP employed TG and 2DPE spectroscopies with exceptional time resolution in the deep UV spectral region. The finding of non-exponential depopulation of the photoexcited 1B state is the primary contribution of this work. We conclude that this non-Markovian behavior is a natural consequence of the coincidence between electronic and nuclear relaxation time scales in α-TP. Kinetic models generally assume that equilibrium is established in the bath on a time scale much shorter than that corresponding to non-radiative transitions in the system. This approximation does not hold in α-TP or the parent molecule, CHD, which also possesses a sub-100 fs internal conversion transition. To our knowledge, α-TP is now the only system in the CHD family of molecules for which the ultrafast internal conversion process between 1B and 2A has been directly time resolved in solution.

It would not be surprising to find similar non-Markovian population transfer dynamics in CHD and its other derivatives (e.g. α-phellandrene). An often-cited 20 fs internal conversion time scale for CHD in solution was determined indirectly using a resonance Raman intensity analysis [15]. We do not dispute this number but suggest that non-Markovian population decay is more consistent with the linear absorption line shape. As in α-TP, the lower-frequency side of the absorbance spectrum of CHD is primarily sensitive to lifetime broadening. Our preliminary model calculations find that the Lorentzian character is greatly overestimated in this region of CHD's absorbance spectrum when a 20 fs exponential decay process is assumed. Future work in our laboratory will directly probe the internal conversion dynamics in CHD and its derivatives with the goal of obtaining more detailed knowledge of the excited state dynamics.

The shape of the anisotropy decay in α-TP suggests that the depopulation of state 1B rapidly accelerates within the first 100 fs after photoexcitation. That is, the population of state 1B follows a Gaussian-like temporal profile for which the magnitude of the first derivative increases from $T = 0$ to 100 fs. Our data suggest that α-TP is subject to two phases of nuclear motions similar to the symmetric and asymmetric geometry changes that take place in the 1B state of CHD [6]. In α-TP, we hypothesize that the excited state wavepacket undergoes several recurrences in the C=C stretching coordinate before displacement along the C=C torsion/vinyl HOOP coordinate finally sets it free from the Franck–Condon region of the 1B potential energy surface. The unconfined wavepacket then transitions from state 1B into state 2A by way of a conical intersection. In support of this interpretation, the Franck–Condon progression of the C=C stretching mode in the linear absorbance spectrum makes clear that the excited state wavepacket recurs 3–4 times at the Franck–Condon geometry before transitioning into the 2A state (i.e. the period of the C=C stretching mode is 23 fs) [65]. In CHD, the photo-initiated wavepacket is known to depart from the 1B state through asymmetric motions. Similarly, based on the observation of a vibrational coherence in our 2DPE data, we suggest that the wavepacket in α-TP leaves the Franck–Condon geometry in the direction of a normal mode involving both C=C torsion and HOOP motion on the vinyl group. The relatively slow onset of the population transfer process at $T = 0$ fs may reflect the suppression of motion along this quasi-out-of-plane coordinate imposed by solvent friction. Theoretical models will be used to establish a more detailed microscopic picture of the dynamics.

Table 4. Model parameters for transient absorption anisotropies.

Parameter[(a)]	$\eta = 4.47$	$\eta = 2.00$
$\mu_{K,1B}$	$0.90\,\mu_{1A,1B}$	$0.90\,\mu_{1A,1B}$
$\mu_{M,2A}$	$1.13\,\mu_{1A,1B}$	$1.13\,\mu_{1A,1B}$
μ_{PP}	$0.60\,\mu_{1A,1B}$	$0.60\,\mu_{1A,1B}$
α	55°	60°
β	65°	60°
θ	40°	40°
τ_1	120 fs	120 fs
τ_2	130 fs	130 fs
τ_{solv}	20 fs	20 fs
τ_{VC}	250 fs	270 fs

[(a)] The model outlined in appendix A.

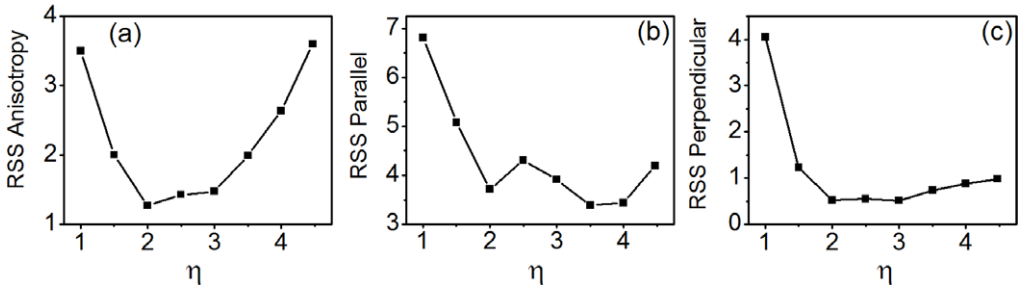

Figure 10. RSS for (a) anisotropy and TG signals acquired with (b) parallel and (c) perpendicular pump and probe electric field polarizations. The RSS in (b) and (c) are divided by 10^8 (i.e. the signal levels are arbitrary). Formulae for the RSS are given in appendix B. It is concluded that the depopulation dynamics of state 1B follow a non-exponential temporal profile in which η ranges from 1.7 to 3.2.

Acknowledgment

This work was supported by the National Science Foundation under grant no. CHE-0952439.

Appendix A. Model for the transient absorption anisotropy

In this appendix, we outline a phenomenological model for the optical response in order to derive further insights from the absorptive TG signals shown in figure 7. The optical response is generally partitioned into three components: the ground state bleach (GSB), excited state emission (ESE) and ESA [20]. The GSB and ESE nonlinearities are fully described in terms of the 1A (ground), 2A and 1B electronic states in α-TP, where this notation is adapted from analogous states in CHD (see figure 2). The ESA signal components involve additional excited states that enter the response only by introducing additional resonances; these higher energy states are never populated in the four-wave mixing process.

Expressions for the GSB signal components are easily generated because the laser spectrum is resonant only with the 1B state (the $\pi\pi^*$ state). The parallel and perpendicular tensor components are given by

$$S_{\parallel}^{\mathrm{GSB}} = \frac{2}{5}\mu_{\mathrm{1B,1A}}^4, \tag{A.1}$$

$$S_{\perp}^{\mathrm{GSB}} = \frac{2}{15}\mu_{\mathrm{1B,1A}}^4, \tag{A.2}$$

where $\mu_{\mathrm{1B,1A}}$ is the magnitude of the transition dipole connecting the 1A ground state to the 1B excited state. The coefficients of $S_{\parallel}^{\mathrm{GSB}}$ and $S_{\perp}^{\mathrm{GSB}}$ represent orientational averages for the isotropic system [66, 67]. The ESE response involves the same four transition dipoles present in the GSB nonlinearity but additionally decays as state 1B transfers population to state 2A. The model must also account for Stokes shifting of the ESE response out of the 36 700–37 900 cm^{-1} spectral window defined by the probe pulse. The reorganization energy determined from fitting the absorbance line shape in section 3.1 suggests that the Stokes shift is in the 2300–3000 cm^{-1} range (i.e. the reorganization energy is approximately half of the Stokes shift) [20], so the measurements lose sensitivity to the ESE nonlinearity during the inertial part of the solvation process. The parallel and perpendicular ESE tensor components are written as

$$S_{\parallel}^{\mathrm{ESE}}(T) = \frac{2}{5}\mu_{\mathrm{1B,1A}}^4 \exp\left[-(T/\tau_1)^{\eta} - (T/\tau_{\mathrm{solv}})^2\right], \tag{A.3}$$

$$S_{\perp}^{\mathrm{ESE}}(T) = \frac{2}{15}\mu_{\mathrm{1B,1A}}^4 \exp\left[-(T/\tau_1)^{\eta} - (T/\tau_{\mathrm{solv}})^2\right], \tag{A.4}$$

where τ_{solv} represents the (Gaussian) inertial solvation dynamics. Notably, τ_{solv} is not the total solvation time scale, rather it represents the (shorter) amount of time needed for the excited state wavepacket to depart from the Franck–Condon geometry. The parameter, η, more directly addresses the depopulation of state 1B than does b in equation (7), because time-coincident electronic and nuclear relaxation processes are disentangled in the present model.

We find that three ESA signal components are needed to fully capture the decay profile of the anisotropy. First, the ESA nonlinearity that decays concomitant with depopulation of state 1B is given by

$${}^{\mathrm{1B}}S_{\parallel}^{\mathrm{ESA}}(T) = \frac{2}{15}\mu_{\mathrm{1B,1A}}^2\mu_{\mathrm{K,1B}}^2[1+2\cos^2(\alpha)]\exp\left[-(T/\tau_1)^{\eta}\right], \tag{A.5}$$

$${}^{\mathrm{1B}}S_{\perp}^{\mathrm{ESA}}(T) = \frac{2}{15}\mu_{\mathrm{1B,1A}}^2\mu_{\mathrm{K,1B}}^2[2-\cos^2(\alpha)]\exp\left[-(T/\tau_1)^{\eta}\right], \tag{A.6}$$

where $\mu_{\mathrm{K,1B}}$ is the magnitude of a transition dipole connecting state 1B to the higher energy state K, and α is the angle between the $\mu_{\mathrm{1B,1A}}$ and $\mu_{\mathrm{K,1B}}$ transition dipoles. Population transfer to the excited state 2A gives rise to a similar ESA nonlinearity

$${}^{\mathrm{2A}}S_{\parallel}^{\mathrm{ESA}}(T) = \frac{2}{15}\mu_{\mathrm{1B,1A}}^2\mu_{\mathrm{M,2A}}^2[1+2\cos^2(\beta)]\{\exp\left(-T/\tau_2\right) - \exp\left[-(T/\tau_1)^{\eta} - T/\tau_2\right]\}, \tag{A.7}$$

$${}^{\mathrm{2A}}S_{\perp}^{\mathrm{ESA}}(T) = \frac{2}{15}\mu_{\mathrm{1B,1A}}^2\mu_{\mathrm{M,2A}}^2[2-\cos^2(\beta)]\{\exp\left(-T/\tau_2\right) - \exp\left[-(T/\tau_1)^{\eta} - T/\tau_2\right]\}. \tag{A.8}$$

These sums of exponentials ensure that ${}^{\mathrm{2A}}S_{\parallel}^{\mathrm{ESA}}(T)$ and ${}^{\mathrm{2A}}S_{\perp}^{\mathrm{ESA}}(T)$ grow when state 2A accepts population from state 1B and decay when state 2A is depopulated. As in the ESA component

associated with state 1B, $\mu_{M,2A}$ is the magnitude of a transition dipole connecting state 2A to state M, and β is the angle between the $\mu_{1B,1A}$ and $\mu_{M,2A}$ transition dipoles. A third ESA signal component is required to obtain an anisotropy that is greater than 0.4 at long delay times. We postulate that the TG measurement is sensitive to the formation of an open-chain photoproduct that (like the regenerated α-TP) undergoes vibrational cooling following ground state recovery. This ESA signal component is written as

$$^{PP}S_{\parallel}^{ESA}(T) = \frac{2}{15}\mu_{1B,1A}^2\mu_{PP}^2[1+2\cos^2(\theta)][1-\exp(-T/\tau_{vc})], \tag{A.9}$$

$$^{PP}S_{\perp}^{ESA}(T) = \frac{2}{15}\mu_{1B,1A}^2\mu_{PP}^2[2-\cos^2(\theta)][1-\exp(-T/\tau_{vc})]. \tag{A.10}$$

The identity of the photoproduct has not been determined, so we write the transition dipole magnitude, μ_{PP}, is a general way. The angle between the $\mu_{1B,1A}$ and μ_{PP} transition dipoles is denoted as θ. $^{PP}S_{\parallel}^{ESA}(T)$ and $^{PP}S_{\perp}^{ESA}(T)$ are taken to depend only on the time constant, τ_{vc}, under the assumption that vibrational cooling is slow compared to the internal conversion process. The main conclusions of this work are insensitive to the inclusion of $^{PP}S_{\parallel}^{ESA}(T)$ and $^{PP}S_{\perp}^{ESA}(T)$ because vibrational cooling is slow compared to internal conversion between 1B and 2A.

Finally, the total parallel and perpendicular signals are obtained by summing the individual components

$$S_{\parallel}^{Total}(T) = -S_{\parallel}^{GSB} - S_{\parallel}^{ESE}(T) + {}^{1B}S_{\parallel}^{ESA}(T) + {}^{2A}S_{\parallel}^{ESA}(T) + {}^{PP}S_{\parallel}^{ESA}(T), \tag{A.11}$$

$$S_{\perp}^{Total}(T) = -S_{\perp}^{GSB} - S_{\perp}^{ESE}(T) + {}^{1B}S_{\perp}^{ESA}(T) + {}^{2A}S_{\perp}^{ESA}(T) + {}^{PP}S_{\perp}^{ESA}(T). \tag{A.12}$$

$S_{\parallel}^{Total}(T)$ and $S_{\perp}^{Total}(T)$ take into account the sign convention used in the transient absorption signals presented in figure 7 (i.e. the bleach has a negative sign). With $S_{\parallel}^{Total}(T)$ and $S_{\perp}^{Total}(T)$ in hand, the anisotropy can be computed using equation (6).

Appendix B. Evaluation of constraints in model calculations

In order to evaluate the sensitivity of the model calculations to the value of η, we carry out an error analysis for both the anisotropy and the individual tensor elements. The residual sum of squares is defined as

$$\mathrm{RSS} = \sum_j (X_{measured}(T_j) - X_{calculated}(T_j))^2, \tag{B.1}$$

where the quantities $X_{measured}(T_j)$ and $X_{calculated}(T_j)$ correspond to $r(T_j)$, $S_{\parallel}(T_j)$ and $S_{\perp}(T_j)$. The delay points, T_j, range from 40 to 600 fs. The residual sum of squares (RSS) determined with our measurements and the model presented in appendix A are displayed in figure 10. Example fits are presented in the bottom row of figure 7. The fitting procedure first sets η equal to the indicated value, and then minimizes the RSS values by varying the other parameters. Fitting the anisotropy together with the two tensor components imposes powerful constraints on the parameters. There is only a small region in parameter space for which reasonable fits are obtained at $T < 0.2$ ps. The angles, α and β, are between 55 and 65°; τ_{solv} is 15–20 fs; the transition dipole magnitudes vary by less than 4% from the values given for $\eta = 2.0$ in table 4. Conservatively, this analysis suggests that the depopulation dynamics of state 1B follow a non-exponential temporal profile in which η ranges from 1.7 to 3.2.

References

[1] Turro N J 1991 *Modern Molecular Photochemistry* (Sausalito, CA: University Science Books)
[2] Nenov A, Kölle P, Robb M A and de Vivie-Riedle R 2010 *J. Org. Chem.* **75** 123
[3] Woodward R B and Hoffmann R 1969 *Angew. Chem. Int. Ed. Engl.* **8** 781
[4] Van der Lugt W T A M and Oosterhoff L J 1969 *J. Am. Chem. Soc.* **91** 6042
[5] Reid P J, Lawless M K, Wickham S D and Mathies R A 1994 *J. Phys. Chem.* **98** 5597
[6] Garavelli M, Page C S, Celani P, Olivucci M, Schmid W E, Trushin S A and Fuss W 2001 *J. Phys. Chem.* A **105** 4458
[7] Deb S and Weber P M 2011 *Annu. Rev. Phys. Chem.* **62** 19
[8] Kosma K, Trushin S A, Fuß W and Schmid W E 2009 *Phys. Chem. Chem. Phys.* **11** 172
[9] Kuthirummal N, Rudakov F M, Evans C L and Weber P M 2006 *J. Chem. Phys.* **125** 133307
[10] Fuß W, Schikarski T, Schmid W E, Trushin S and Kompa K L 1996 *Chem. Phys. Lett.* **262** 675
[11] Anderson N A, Pullen S H, Walker L A, Shiang J J and Sension R J 1998 *J. Phys. Chem.* A **102** 10588
[12] Pullen S H, Anderson N A, Walker L A and Sension R J 1998 *J. Chem. Phys.* **108** 556
[13] Lochbrunner S, Fuss W, Schmid W E and Kompa K L 1998 *J. Phys. Chem.* A **102** 9334
[14] Pullen S H, Walker L A, Donovan B and Sension R J 1995 *Chem. Phys. Lett.* **242** 415
[15] Trulson M O, Dollinger G D and Mathies R A 1989 *J. Chem. Phys.* **90** 4274
[16] Kim J, Tao H, White J L, Petrovic V S, Martinez T J and Bucksbaum P H 2012 *J. Phys. Chem.* A **116** 2758
[17] Minaard N G and Havinga E 1973 *Recl. Trav. Chim. Pays-Bas* **92** 1315
[18] Rudakov F and Weber P M 2009 *Chem. Phys. Lett.* **470** 187
[19] Nitzan A 2006 *Chemical Dynamics in Condensed Phases* (Oxford: Oxford University Press)
[20] Mukamel S 1995 *Principles of Nonlinear Optical Spectroscopy* (New York: Oxford University Press)
[21] Worth G A and Cederbaum L S 2004 *Annu. Rev. Phys. Chem.* **55** 127
[22] Domcke W, Yarkony D and Köppel H 2011 *Conical Intersections: Theory Computation and Experiment* (Singapore: World Scientific)
[23] Farrow D A, Qian W, Smith E R, Ferro A A and Jonas D M 2008 *J. Chem. Phys.* **128** 144510
[24] Yetzbacher M K, Belabas N, Kitney K A and Jonas D M 2007 *J. Chem. Phys.* **126** 044511
[25] Zimdars D, Francis R S, Ferrante C and Fayer M D 1997 *J. Chem. Phys.* **106** 7498
[26] Reuther A, Iglev H, Laenen R and Laubereau A 2000 *Chem. Phys. Lett.* **325** 360
[27] Selig U, Schleussner C-F, Foerster M, Langhojer F, Nuernberger P and Brixner T 2010 *Opt. Lett.* **35** 4178
[28] Tseng C-H, Matsika S and Weinacht T C 2009 *Opt. Express* **17** 18788
[29] West B A, Womick J M and Moran A M 2011 *J. Phys. Chem.* A **115** 8630
[30] West B A and Moran A M 2012 *J. Phys. Chem. Lett.* **3** 2575
[31] West B A, Womick J M and Moran A M 2011 *J. Chem. Phys.* **135** 114505
[32] Durfee C G, Backus S, Murnane M M and Kapteyn H C 1997 *Opt. Lett.* **22** 1565
[33] Durfee C G, Misoguti L, Backus S, Kapteyn H C and Murnane M M 2002 *J. Opt. Soc. Am.* B **19** 822
[34] Durfee C G, Backus S, Kapteyn H C and Murnane M M 1999 *Opt. Lett.* **24** 697
[35] Nubling R K and Harrington J A 1998 *Opt. Eng.* **37** 2454
[36] Saito M, Sato S-Y and Miyagi M 1993 *J. Opt. Soc. Am.* A **10** 277
[37] Jailaubekov A E and Bradforth S E 2005 *Appl. Phys. Lett.* **87** 021107
[38] Rivera C A, Bradforth S E and Tempea G 2010 *Opt. Express* **18** 18615
[39] Brixner T, Mancal T, Stiopkin I V and Fleming G R 2004 *J. Chem. Phys.* **121** 4221
[40] Lepetit L, Chériaux G and Joffre M 1995 *J. Opt. Soc. Am.* B **12** 2467
[41] Gallagher S M, Albrecht A W, Hybl J D, Landin B L, Rajaram B and Jonas D M 1998 *J. Opt. Soc. Am.* B **15** 2338
[42] Tauber M J, Mathies R A, Chen X and Bradforth S E 2003 *Rev. Sci. Instrum.* **74** 4958
[43] Reid P J, Doig S J and Mathies R A 1990 *J. Phys. Chem.* **94** 8396
[44] Merchán M, Serrano-Andrés L, Slater L S, Roos B O, McDiarmid R and Xing X 1999 *J. Phys. Chem.* A **103** 5468

[45] Fleming G R 1986 *Chemical Applications of Ultrafast Spectroscopy* (New York: Oxford University Press)
[46] Wynne K and Hochstrasser R M 1993 *Chem. Phys.* **171** 179
[47] Qian W and Jonas D M 2003 *J. Chem. Phys.* **119** 1611
[48] Tamura H, Nanbu S, Ishida T and Nakamura H 2006 *J. Chem. Phys.* **124** 084313
[49] Hofmann A and de Vivie-Riedle R 2000 *J. Chem. Phys.* **112** 5054
[50] Jonas D M 2003 *Annu. Rev. Phys. Chem.* **54** 425
[51] Frisch M J *et al* 2009 *Gaussian 09 Revision C.01* (www.gaussian.com)
[52] Collini E and Scholes G D 2009 *Science* **323** 369
[53] Engel G S, Calhoun T R, Read E L, Ahn T K, Mancal T, Cheng Y C, Blankenship R E and Fleming G R 2007 *Nature* **446** 782
[54] Christensson N, Milota F, Hauer J, Sperling J, Bixner O, Nemeth A and Kauffmann H F 2011 *J. Phys. Chem.* B **115** 5383
[55] Karaiskaj D, Bristow A D, Yang L, Dai X, Mirin R P, Mukamel S and Cundiff S T 2010 *Phys. Rev. Lett* **104** 117401
[56] Cho M 2008 *Chem. Rev.* **108** 1331
[57] Pakoulev A V, Block S B, Yurs L A, Mathew N A, Kornau K M and Wright J C 2010 *J. Phys. Chem. Lett.* **1** 822
[58] Ogilvie J P and Kubarych K J 2009 *Adv. At. Mol. Opt. Phys.* **57** 249
[59] Turner D B and Nelson K A 2010 *Nature* **466** 1089
[60] Lott G A, Perdomo-Ortiz A, Utterback J K, Widom J R, Aspuru-Guzik A and Marcus A H 2011 *Proc. Natl Acad. Sci. USA* **108** 16521
[61] Hamm P and Zanni M T 2011 *Concepts and Methods of 2D Infrared Spectroscopy* (Cambridge: Cambridge University Press)
[62] Richards G H, Wilk K E, Curmi P M G, Quiney H M and Davis J A 2012 *J. Phys. Chem. Lett.* **3** 272
[63] Caram J R, Lewis N H C, Fidler A F and Engel G S 2012 *J. Chem. Phys.* **136** 104505
[64] Tseng C-H, Sándor P, Kotur M, Weinacht T C and Matsika S 2012 *J. Phys. Chem.* A **116** 2654
[65] Heller E J 1981 *Acc. Chem. Res.* **14** 368
[66] Hochstrasser R M 2001 *Chem. Phys.* **266** 273
[67] Dreyer J, Moran A M and Mukamel S 2003 *Bull. Korean Chem. Soc.* **24** 1091
[68] Wiberg K and Shrake A 1973 *Spectrochim. Acta* A **29** 583